Journal of Control, Automation and Electrical Systems, Available online 18 January 2026
DOI: 10.1007/s40313-025-01234-w

Design of a Robust Adaptive Neural Network MPPT Controller for a Photovoltaic Energy Storage System

Ahsene Boubakir[1*], Mourad Aït Ahmed[2†], Salim Labiod[1†], Toufik Souanef[3†]

[1*]University of Jijel, LAJ, Faculty of Science and Technology, BP. 98, Ouled Aissa, 18000, Jijel, Algeria.
[2]Nantes Université, Institut de Recherche en Energie Electrique de Nantes Atlantique, IREENA, UR 4642, F-44600, Saint-Nazaire, France.
[3]Cranfield University, School of Aerospace Transport and Manufacturing, MK43 0AL, College Road, Cranfield, UK.

*Corresponding author(s). E-mail(s): ahsene.boubakir@univ-jijel.dz;
Contributing authors: mourad.ait-ahmed@univ-nantes.fr; salim.labiod@univ-jijel.dz; toufik.souanef@cranfield.ac.uk;
†These authors contributed equally to this work.

Abstract

This paper presents the design of an $\mathcal{L}_1$ Adaptive Neural Network (ANN) Maximum Power Point Tracking (MPPT) controller for a Photovoltaic Energy Storage (PV-ES) system consisting of a PV module, a DC–DC boost converter, and a battery storage unit. The controller combines the $\mathcal{L}_1$ adaptive control method with a Radial Basis Function (RBF) neural network to approximate unknown nonlinear dynamics and compensate for system uncertainties. This integration enables fast adaptation while preserving robustness, thereby overcoming key limitations of conventional MPPT strategies. Simulation results demonstrate that the proposed $\mathcal{L}_1$ ANN-MPPT controller ensures rapid convergence to the maximum power point, reduced steady-state oscillations, and enhanced battery charging efficiency under highly variable irradiance and temperature conditions. These findings quantitatively confirm that the proposed controller eliminates the conventional trade-off between dynamic response and steady-state precision, offering superior speed, stability, and accuracy in maximum power point tracking. Overall, the results validate its effectiveness and highlight its potential for real-time deployment in renewable energy systems.

Published by Springer. This is the Author Accepted Manuscript issued with: Creative Commons Attribution License (CC:BY 4.0).
The final published version (version of record) is available online at DOI:10.1007/s40313-025-01234-w. Please refer to any applicable publisher terms of use.

Keywords: Photovoltaic system, storage battery, $\mathcal{L}_1$ adaptive control, MPPT controller, fast adaptation, RBF neural network.

1 Introduction

In recent years, solar energy has garnered increasing attention, mainly due to the urgent need to reduce carbon emissions and combat climate change, prompting many countries to explore renewable energy sources (Smets et al., 2016; Reinders et al., 2017). Moreover, technological advancements have improved the efficiency of solar panels while simultaneously reducing costs, making this energy source more accessible to households and businesses alike. Additionally, government incentives, such as subsidies and feed-in tariffs, have further encouraged the adoption of solar energy. As a result, the importance of solar energy in the transition towards a sustainable energy future is becoming increasingly apparent, addressing growing energy demands while minimising environmental impact (Pourasl et al., 2023).

PV generator systems are purposefully engineered to transform solar energy into electricity efficiently and at a low cost (Smets et al., 2016). These systems can be classified into two distinct types (Boubakir et al., 2021, 2022): autonomous or standalone systems, which are employed for purposes such as battery charging and water pumping, and grid-connected systems. PV systems capture solar energy and convert it directly into electrical power through semiconductor devices called PV cells, which operate based on the photovoltaic effect. The capability to generate electricity directly from sunlight makes PV systems an exceptionally advantageous and flexible solution for a variety of energy needs (Pourasl et al., 2023). A PV-ES system is designed to capture and retain excess solar energy for later use, providing a reliable power supply, especially during times of reduced sunlight or power failures (Kaldellis, 2015; Yatimi and Aroudam, 2016; Maka and Chaudhary, 2024). This system consists of solar panels, a storage battery, a charge controller, and a converter. It plays a significant role in enhancing energy efficiency and promoting the transition to renewable energy sources. The efficiency of a PV-ES system is contingent upon multiple key factors (Yatimi and Aroudam, 2016; Kuvshinov et al., 2019): the quality and operational performance of the solar panels, the type and capacity of the storage battery, and the efficiency of both the converters and the MPPT controllers. The MPPT controller is essential in a PV-ES system, as it optimizes the generation of electricity. It consistently modifies the operating point of solar panels to ensure they produce the highest possible power, regardless of changes in sunlight and temperature (Sarvi and Azadian, 2022). By maximizing the energy generated, the MPPT improves battery storage efficiency and ensures effective management of interactions with the load or the electrical grid.

The literature presents a variety of MPPT controller types, each with distinct advantages and drawbacks (Jately and Arora, 2017; Mao et al., 2020; Jately et al., 2021; Sarvi and Azadian, 2022; Chen et al., 2024; Harrison et al., 2025). The Perturb and Observe (P&O) algorithm (Mao et al., 2020; Eltamaly, 2018; Chatterjee and Mahato, 2024) is one of the most commonly used methods; its principle involves continuously adjusting the voltage to achieve optimal power extraction. The primary

drawback of the P&O MPPT controller is its tendency to induce oscillations around the Maximum Power point (MPP), which can result in power losses during steady-state operation. Furthermore, it exhibits a slow response to rapid changes in sunlight conditions and may occasionally track an incorrect MPP, particularly in environments characterized by swift fluctuations. Another significant approach is the Incremental Conductance (IC) method (Safari and Mekhilef, 2011; Loukriz et al., 2016), which compares the incremental conductance to the instantaneous conductance to locate the MPP. The IC MPPT controller presents a significant challenge in terms of implementation complexity, as it requires the simultaneous calculation of instantaneous and incremental conductance. Moreover, despite its superior accuracy relative to the P&O method, its effectiveness can be compromised by noise or instabilities in measurements, which may result in inaccuracies in identifying the MPP. The Hill-Climbing (HC) algorithm operates by perturbing the duty cycle or the voltage of the PV array and observing the resulting change in output power (Jately and Arora, 2016, 2018; Jately et al., 2021). If the power increases, the perturbation is continued in the same direction; otherwise, the direction is reversed. Although conceptually simple and easy to implement, the conventional HC algorithm suffers from drawbacks similar to those of the P&O technique. Other methodologies include fuzzy logic control (Ali et al., 2022; Bharti et al., 2024), which applies a set of rules to address uncertainties, and algorithms based on neural networks (Messalti et al., 2017; Tchouani Njomo et al., 2021; El Mezdi et al., 2023) that learn to forecast the MPP based on varying input conditions. Additionally, newer methods, such as those grounded in evolutionary algorithms (Swetha et al., 2023; Sameera et al., 2024), are starting to gain traction in the literature. While MPPT controllers employing evolutionary algorithms and Artificial Intelligence (AI) are efficient, they encounter several limitations (Yap et al., 2020; Raj and Samuel, 2022), including computational complexity, potential delays in convergence, the danger of being trapped in local optima, and the requirement for high-level technical expertise. Moreover, the implementation of AI is contingent upon the availability of training data, which can further complicate their use. In this context, sensorless approaches have emerged as promising alternatives, since they avoid reliance on additional climatic sensors and often simplify system implementation. Several studies have reported effective frameworks and models that eliminate the dependency on environmental sensors while maintaining reliable PV system performance as in Harrison et al. (2025); Wei et al. (2025); Harrison et al. (2026).

In recent times, academic literature has introduced MPPT controllers that incorporate advanced control techniques, including sliding mode (Yatimi and Aroudam, 2016; Inthamoussou and Valenciaga, 2021), adaptive control (Manna et al., 2023), backstepping (Arsalan et al., 2018; Belghiti et al., 2024), and predictive control (Lashab et al., 2017; Ahmed et al., 2023). This growing interest is driven by the need to improve MPPT efficiency compared to traditional MPPT controllers. While conventional methods may perform adequately under typical conditions, they often exhibit deficiencies in robustness, response speed, and accuracy when faced with dynamic conditions or significant disturbances (Yatimi and Aroudam, 2016). PV-ES systems exhibit rapid dynamics and generally function under fluctuating atmospheric conditions. Therefore, to improve the MPPT performance, it is essential to adopt a robust MPPT controller

with significant self-adaptive capability. The major advantage of the $\mathcal{L}_1$ adaptive control method, whose principle is well presented in Hovakimyan and Cao (2010), compared to conventional adaptive control methods, lies in its ability to decouple the adaptation process from control performance (Boubakir et al., 2022; Hovakimyan and Cao, 2010; Boubakir et al., 2016). This feature enables rapid adaptation while maintaining stability and robustness. Inspired by the preceding discussion, this research presents an $\mathcal{L}_1$ ANN-MPPT controller that allows for rapid adaptation without sacrificing robustness. The proposed MPPT controller combines a control law, a predictor, and an adaptive mechanism, along with an RBF neural network to address unknown nonlinear dynamics and uncertainties throughout the system, further enhancing state prediction and, consequently, MPP tracking performance.

The primary benefits of the introduced $\mathcal{L}_1$ ANN-MPPT controller, along with this paper's key contributions, are as follows:

1. The low-pass filter incorporated into the control channel allows for the separation of the estimation loop from the control loop. Consequently, the resulting $\mathcal{L}_1$ ANN-MPPT controller enables rapid adaptation without compromising robustness, positioning it as an effective approach for controlling the MPP in PV-ES systems known for their fast dynamics.
2. In contrast to conventional NN-based MPPT controllers, the neural network in our design is not employed as a standalone decision-making element but rather as an adaptive estimator within the $\mathcal{L}_1$ control law structure. Specifically, the RBF neural network approximates uncertain system nonlinearities and external disturbances, thereby reducing state prediction errors and enhancing control accuracy, while avoiding the instability risks often associated with purely NN-based methods.
3. The established MPPT control approach maintains uniform performance bounds for the system's inputs and outputs relative to a stable virtual reference system. This implies that, apart from ensuring steady-state tracking, the $\mathcal{L}_1$ ANN-MPPT controller is also capable of ensuring that the transient response remains predictable and bounded.
4. In contrast to conventional MPPT controllers, such as P&O methods (Mao et al., 2020; Eltamaly, 2018) and IC methods (Safari and Mekhilef, 2011; Loukriz et al., 2016), and newer controllers that use artificial intelligence tools like fuzzy logic (Ali et al., 2022; Bharti et al., 2024), neural networks (Messalti et al., 2017; Tchouani Njomo et al., 2021; El Mezdi et al., 2023), or those developed using evolutionary optimization algorithms (Swetha et al., 2023; Sameera et al., 2024) or advanced control techniques (Yatimi and Aroudam, 2016; Inthamoussou and Valenciaga, 2021; Manna et al., 2023; Arsalan et al., 2018; Belghiti et al., 2024; Lashab et al., 2017; Ahmed et al., 2023) the proposed $\mathcal{L}_1$ ANN-MPPT controller ensures effective MPP tracking with significant self-adjusting capabilities while maintaining robustness.

The remainder of this paper is outlined as follows: Section 2 provides the description and modeling of the investigated PV-ES system. Section 3 presents the design of the proposed $\mathcal{L}_1$ ANN-MPPT controller. Section 4 examines the stability and performance of the proposed MPPT controller. The capability and operational efficiency of the

$\mathcal{L}_1$ ANN-MPPT controller are analyzed in Section 5 through a series of numerical simulations and comparative analyses. Section 6 concludes the study by summarising the findings.

2 Analysis and modeling of the investigated PV-ES system

The system under study is illustrated schematically in Figure 1. It includes a PV module, a DC-DC boost converter and a battery storage system. These components work together synergistically to harvest solar energy efficiently, store it for later use, and ensure the smooth operation of the PV-ES system (Yatimi and Aroudam, 2016; Kuvshinov et al., 2019). The PV module is the primary component responsible for converting sunlight into electricity through the photovoltaic effect (Smets et al., 2016; Boubakir et al., 2021, 2022). The battery serves as an energy storage device in the system; it stores excess electricity generated by the PV module during periods of sunlight for later use when sunlight is not available. The boost converter, with its MPPT control mechanism, maximizes the amount of power extracted from the sunlight falling on the panels. The MPPT controller also plays a crucial role in efficiently charging the batteries. By optimizing the power output of the solar panels, the MPPT controller ensures that the batteries receive the maximum amount of charge possible, resulting in quicker charging times and enhanced overall system performance.

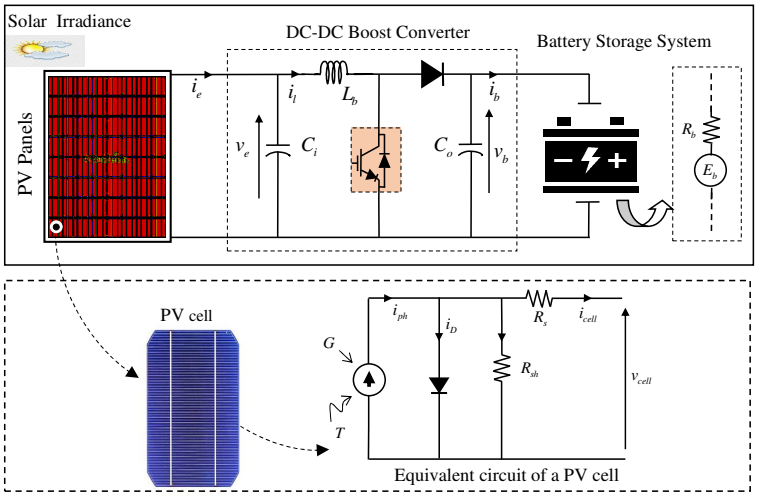


Fig. 1 Schematic diagram of the investigated PV-ES system.

2.1 Modeling of the PV module

PV cells are essential components found in all PV generator systems (Smets et al., 2016). They function as p–n junctions, enabling the direct conversion of sunlight into electrical power. Illustrated in Figure 1, the equivalent circuit model of a PV cell

comprises a light-generated current source in parallel with a diode, as well as a series resistance (R_s) and a shunt resistance (R_{sh}). The components R_s and R_{sh} characterize internal losses and parallel leakage pathways, respectively. Recognizing that a single PV cell can only provide a limited amount of energy, multiple cells are arranged in series-parallel configurations to create a PV module capable of generating higher current and voltage levels. The combination of these PV modules, interconnected in both series and parallel, forms a PV generator, facilitating the achievement of the desired output power.

The essential behavior of a PV module, comprising n_s cells in series and n_p cells in parallel, across various operational conditions, can be described by (Yatimi and Aroudam, 2016; Boubakir et al., 2021, 2022):

$$i_e = n_p i_{ph} - n_p I_0 \left[exp\left(\left(\frac{q_e}{n_s d_f K_b T} \right) \left(v_e + \frac{n_s}{n_p} R_s i_e \right) \right) - 1 \right] - \frac{n_p}{R_{sh}} \left(\frac{v_e}{n_s} + \frac{R_s}{n_p} i_e \right) \tag{1}$$

where i_e and v_e denote the current and voltage of the PV module, q_e is the electron charge $\left(q_e = 1,6 \times 10^{-19}\, C\right)$, d_f is the ideality factor of the diode, K_b is the Boltzmann constant $\left(K_b = 1,38 \times 10^{-23}\, J/K\right)$, T is the cell temperature. The currents i_{ph} and I_0 represent, respectively, the PV current and the cell reverse saturation current, and they are expressed as (Boubakir et al., 2021, 2022):

$$i_{ph} = \left(i_{sc} + K_{sc}\left(T - T_r\right)\right) \frac{G}{1000} \tag{2}$$

$$I_0 = I_{0R} \left[\frac{T}{T_r} \right]^3 exp\left[\frac{q_e E_g}{d_f K_b} \left(\frac{1}{T_r} - \frac{1}{T} \right) \right] \tag{3}$$

with i_{sc} is the short circuit current under standard temperature and radiation conditions, K_{sc} is the short circuit current temperature coefficient, T_r denotes the reference temperature, I_{0R} is the reverse saturation current at T_r. G stands for the total solar radiation in W/m^2, and E_g represents the band gap of the semiconductor employed in the cell.

2.2 Averaged modeling of the boost converter linked to the battery storage

The boost converter plays a crucial role in power electronics, primarily focusing on increasing voltage while simultaneously decreasing current levels to enhance power transfer efficiency. It serves as a vital link between PV modules and loads or batteries, employing semiconductor switches like a diode and a transistor, in addition to essential components such as an inductor and input/output capacitors. These elements work together to regulate energy flow, ensuring that the PV module operates at its MPP to optimize energy output.

The average dynamic model (4) encompasses the combined behavior of the boost converter operating in continuous conduction mode and the battery storage system. It captures the fundamental dynamics of both components while omitting intricate

details, thereby facilitating analysis and design (Yatimi and Aroudam, 2016), and can be expressed as follows:

$$\begin{cases} C_i \frac{dv_e}{dt} = i_e - i_l \\ L_b \frac{di_l}{dt} = v_e - (1-\alpha)\, v_b \\ C_o \frac{dv_b}{dt} = \frac{v_b}{R_b} - \frac{E_b}{R_b} + (1-\alpha)\, i_l \end{cases} \tag{4}$$

where i_e and v_e stand for the output current and voltage of the PV generator, while i_l indicates the current flowing through the inductor. v_b represents the output voltage of the boost converter, and C_i refers to the input capacitor. L_b denotes the inductance of the boost converter, and C_o represents the output capacitor. α is used to denote the duty cycle of the boost converter and it represents the proportion of time during which the switching element of the boost converter is active, relative to the entire switching period. As illustrated in (1), the battery is viewed as a constant voltage source E_b linked in series with a constant resistance R_b (Yatimi and Aroudam, 2016): $v_b = E_b + R_b \cdot i_b$.

The state representation of the average dynamic model (4) can be expressed as

$$\begin{cases} \frac{dx_1}{dt} = \frac{i_e}{C_i} - \frac{1}{C_i} x_2 \\ \frac{dx_2}{dt} = \frac{1}{L_b} x_1 - \frac{x_3}{L_b} u \\ \frac{dx_3}{dt} = \frac{E_b}{C_o R_b} - \frac{1}{C_o R_b} x_3 + \frac{x_2}{C_o} u \end{cases} \tag{5}$$

where $x_1 = v_e$, $x_2 = i_l$, $x_3 = v_b$ and $u = 1 - \alpha$ stand for the control input.

3 Design of an $\mathcal{L}_1$ ANN-MPPT Controller

This section thoroughly explores the various stages involved in designing an $\mathcal{L}_1$ ANN-MPPT controller. The proposed MPPT controller comprises a predictor, a control law with its adaptive law, and incorporates an RBF neural network to serve the purpose of function approximation. This approach marks a departure from conventional MPPT methods, presenting an efficient solution for enhancing the performance of PV systems. Our objective is to develop a robust and rapid MPPT controller capable of dynamically adjusting the system's operating point to consistently harness maximum power under various weather conditions.

3.1 Problem statement

The design of the proposed MPPT technique revolves around a fundamental observation: at the MPP, the slope of the power-voltage characteristic curves, represented by $\frac{\partial P}{\partial v_e}$, reaches zero. Mathematically, this relationship can be articulated as follows (Yatimi and Aroudam, 2016):

$$\left.\frac{\partial P_e}{\partial v_e}\right|_{MPP} = \frac{\partial (v_e \times i_e)}{\partial v_e} = i_e + v_e \frac{\partial i_e}{\partial v_e} = 0 \tag{6}$$

Hence, in order to fulfill the control objective, we designate y as the system output to be driven to zero within a finite time. This output is defined as follows:

$$y = \frac{\partial P_e}{\partial v_e} = i_e + v_e \frac{\partial i_e}{\partial v_e} \tag{7}$$

Based on the preceding analysis, we can express the input-output representation of the average dynamic model (5) as follows:

$$\ddot{y} = f(x,t) + g(x,t)\, u \tag{8}$$

where $f(x,t)$ and $g(x,t)$ are given by (Yatimi and Aroudam, 2016) :

$$f(x,t) = \left(\frac{\partial^3 P_e}{\partial v_e^3}\right)\left(\frac{\partial v_e}{\partial t}\right)^2 + \frac{1}{C_i}\left(\frac{\partial^2 P_e}{\partial v_e^2}\right)\left[\left(\frac{\partial i_e}{\partial v_e}\right)\left(\frac{\partial v_e}{\partial t}\right) - \frac{v_e}{L_b}\right] \tag{9}$$

$$g(x,t) = \frac{1}{C_i}\left(\frac{\partial^2 P_e}{\partial v_e^2}\right)\frac{v_b}{L_b} \tag{10}$$

with

$$\begin{cases} \frac{\partial^2 P_e}{\partial v_e^2} = 2\frac{\partial i_e}{\partial v_e} + v_e \frac{\partial^2 i_e}{\partial v_e^2} \\ \frac{\partial^3 P_e}{\partial v_e^3} = 3\frac{\partial^2 i_e}{\partial v_e^2} + v_e \frac{\partial^3 i_e}{\partial v_e^3} \end{cases} \tag{11}$$

Given that the input-output model in (8) has a relative degree of 2, we define a sliding surface σ as follows:

$$\sigma = \dot{y} + \lambda y \tag{12}$$

where $\lambda > 0$. We deduce from (12) that the solution of the linear differential equation $\sigma = 0$ indicates that both the output y and its derivative $\dot{y}$ tend towards zero. Additionally, constraints on σ can be straightforwardly translated into bounds on y and $\dot{y}$ (Slotine and Li, 1991; Boubakir et al., 2014). To elaborate, if $|\sigma| \leq \mathcal{O}$, where $\mathcal{O}$ represents a positive constant, we can infer that $y^{(r)}(t) \leq 2^r \lambda^{r-1} \mathcal{O}$, $r = 0, 1$.

Based on (8), we can depict the dynamics of σ as follows:

$$\dot{\sigma} = f(x,t) + g(x,t)\, u + \lambda \dot{y} \tag{13}$$

By definition of a signal δ such that $\delta = \lambda \dot{y} + \beta \sigma$ with $\beta > 0$, the dynamics (13) can also be expressed by

$$\dot{\sigma} = -\beta \sigma + f(x,t) + g(x,t)\, u + \delta \tag{14}$$

It is evident that, for the unknown nonlinear term $g(x,t)\, u$ in (14), there are always Δ and $\Psi(x,u)$ that satisfy the condition that

$$g(x,t)\, u = -\Delta u + \Psi(x,u) \tag{15}$$

Here, Ψ represents the discrepancy between $g(x,t)u$ and Δu, where Δ is an unknown positive constant assumed to be bounded and positive, such that $0 < g_1 < \Delta < g_2$, with g_1 and g_2 being positive constants. Since the input–output gain $g(x,t)$ in (10) depends only on PV quantities evolving within bounded physical limits, the function

$g(x,t)$ is naturally bounded. Hence, g_1 and g_2 represent theoretical positive bounds whose numerical values are not required; only their existence, which ensures that $0 < g_1 < \Delta < g_2$, is needed for the design of the proposed $\mathcal{L}_1$ ANN-MPPT control law.

By substituting (15) in (14) and defining $H(x,u,\delta)$ as $H(x,u,\delta) = f(x,t) + \Psi(x,u) + \delta$, it results

$$\dot{\sigma} = -\beta\sigma - \Delta u + H(x,u,\delta) \tag{16}$$

Given that the nonlinear function $H(x,u,\delta)$ in (16) is unknown, our approach in this study involves utilizing an RBF neural network to approximate this term.

3.2 Description of the employed RBF neural networks approximator

The commendable function approximation capabilities, adaptability, and straightforward structure of RBF neural networks have allowed them to play a crucial role in adaptive controllers design (Sanner and Slotine, 1992; Boubakir and Labiod, 2023). These neural networks, characterized by linear parameterization, can be easily designed and implemented. In this work, a Gaussian RBF neural network is employed to closely approximate the function H. The effectiveness of Gaussian RBF neural networks in approximating arbitrary continuous functions has been established (Sanner and Slotine, 1992; Chen and Chen, 1995). The output of the considered RBF neural networks approximator can be computed as

$$y_n(\pi) = w^T \psi(\pi) \tag{17}$$

where $\pi \in \Omega_\pi \subset \mathbb{R}^q$ denotes the input vector, $w = [w_1, w_2, \cdots, w_z]^T \in \mathbb{R}^z$ are the weights vector, $z > 1$ is the neural network node number and $\psi(\pi) = [\psi_1(\pi), \psi_2(\pi), \cdots, \psi_z(\pi)]^T$ designates a vector of Gaussian RBF given by (Boubakir and Labiod, 2023):

$$\psi_i(\pi) = exp\left[-\frac{(\pi - a_i)^T(\pi - a_i)}{b_i^2}\right],\ i = 1, \ldots, z \tag{18}$$

here, $a_i = [a_{i1}, a_{i2}, \cdots, a_{iq}]^T$ represents the center of the receptive vector and b_i denotes the width of the Gaussian function.

3.3 $\mathcal{L}_1$ ANN-MPPT control architecture

Now, we describe in detail the architecture of the developed $\mathcal{L}_1$ ANN-MPPT controller. Initially, based on the universal approximation theorem (Sanner and Slotine, 1992; Chen and Chen, 1995), we hypothesize that the nonlinear term $H(x,u,\delta)$ can be closely approximated over a compact set by an RBF neural network as follows

$$H(x,u,\delta) = w^T \psi(\pi) + \epsilon(\pi), |\epsilon(\pi)| < \epsilon^\star \tag{19}$$

where π denotes the input vector of the RBF neural network and ϵ represents the approximation error, which is assumed to be bounded such that $|\epsilon| \leq \epsilon^\star$, with $\epsilon^\star$ being a positive constant.

Now, by substituting (19) into (16), one can obtain the following closed-loop dynamics

$$\dot{\sigma} = -\beta\sigma - \Delta u + w^T \psi(\pi) + \epsilon(\pi), \sigma(0) = \sigma_0 \tag{20}$$

At this point, we present the key components of the designed MPPT controller, followed by an assessment of its effectiveness. To begin, we define the predictor (21) which replicates the dynamics in (20), with the unknown terms Δ and w substituted by their estimates $\hat{\Delta}$ and $\hat{w}$, respectively, as

$$\dot{\hat{\sigma}} = -\beta\hat{\sigma} - \hat{\Delta} u + \hat{w}^T \psi(\pi), \hat{\sigma}(0) = \sigma_0 \tag{21}$$

where $\hat{\sigma} \in R$ denotes the estimation of the sliding surface $\sigma(t)$. The terms $\hat{\Delta}$ and $\hat{w}$ are determined by the subsequent projection-type adaptation laws

$$\begin{cases} \dot{\hat{\Delta}} = \Gamma Proj\left(\hat{\Delta}, \tilde{\sigma} u\right) \\ \dot{\hat{w}} = \Gamma Proj\left(\hat{w}, -\tilde{\sigma}\psi(\pi)\right) \end{cases} \tag{22}$$

where $\tilde{\sigma}$ stands for the prediction error such that $\tilde{\sigma} = \hat{\sigma} - \sigma$, Γ represents the adaptation gain and $Proj(\cdot, \cdot)$ denotes the projection operator (see Appendix B).

As for the control law, we choose its structure as follows :

$$u = KD(p)\eta(p) \tag{23}$$

here p denotes the complex variable, $\eta(p)$ denotes the Laplace transform of $\eta(t)$ defined as $\eta(t) = -\hat{\Delta} u + \hat{w}^T \psi(\pi)$, K serves as a feedback gain, $D(p)$ is chosen as a strictly proper transfer function to achieve stability in the resulting closed-loop filter, denoted $C(p)$, such that

$$C(p) = \frac{\Delta K D(p)}{1 + \Delta K D(p)} \tag{24}$$

Accordingly, the form of the closed-loop filter $C(p)$ can represent a first order low-pass filter when the transfer function $D(p)$ is selected as $D(p) = \frac{1}{p}$, leading to

$$C(p) = \frac{\Delta K}{p + \Delta K} \tag{25}$$

with DC gain $C(0) = 1$.

Prior to introducing the stability analysis of the suggested $\mathcal{L}_1$ ANN-MPPT controller, we present the subsequent assumption concerning the function $H(x, u, \delta)$:

Assumption 1. Given that the state vector $x(t)$ exhibits comparable stability and boundedness characteristics to $\sigma(t)$, the subsequent boundary can be deemed reasonable

$$|H(x, u, \delta)| \leq L|\sigma| + L_0 \tag{26}$$

where L_1 and L_2 are some positive constants. ⊡

Remark 1. *In Assumption 1, we assume that the uncertain quantity $H(x,u,\delta)$ is bounded above by a functional bound. Consequently, considering the bound in equation (26), it becomes evident that it is not constant; instead, it increases as the sliding surface $\sigma(t)$ tends toward infinity. This characteristic renders this assumption physically acceptable.* ⊡

The schematic representation of the proposed $\mathcal{L}_1$ ANN-MPPT controller is illustrated in Figure 2. The control input u for the system described by (8) is determined by the control law given in (23), incorporating a predictor outlined in (21), and an adaptive law specified by (22). To ensure stability, the design parameters λ and the filter $C(p)$ are chosen such that the condition for the $\mathcal{L}_1$-norm is satisfied, as expressed in (27):

$$\|Q(p)\|_{\mathcal{L}_1} L < 1 \tag{27}$$

where $Q(p) = M(p)(1 - C(p))$, $M(p) = (p+\beta)^{-1}$ and L is introduced in (26). Let us point out here that both functions $M(p)$ and $Q(p)$ are proper BIBO-stable transfer functions as long as the design parameter β is strictly positive and the filter $C(p)$ is a BIBO-stable strictly proper transfer function .

Remark 2. *In this approach, the design parameters λ and β are employed to define the desired closed-loop dynamics, while the feedback gain K can be adjusted to tune the bandwidth-limited filter $C(p)$. Within a specified frequency range, this filter plays a crucial role in ensuring accurate tracking of reference signals and improving robustness against uncertainties.* ⊡

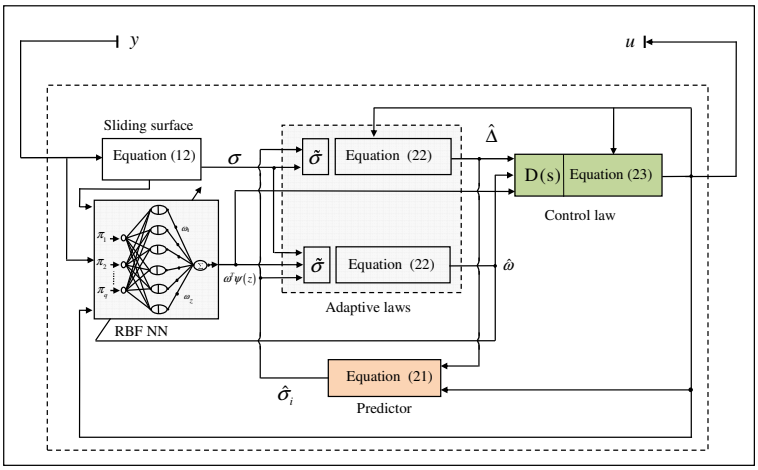


Fig. 2 Block diagram of the suggested $\mathcal{L}_1$ ANN-MPPT controller.

4 Analysis of the $\mathcal{L}_1$ ANN-MPPT controller

4.1 Ideal closed-loop reference system

We introduce a well-behaved closed-loop reference system and provide proof of its stability. The structure of the closed-loop reference system is outlined below

$$\begin{cases} \dot{\sigma}_r = -\beta\sigma_r - \Delta u_r + w^T\psi\left(\pi_r\right) + \epsilon\left(\pi_r\right), \sigma_r\left(0\right) = \sigma_0 \\ u_r = \frac{C(p)}{\Delta}\eta_r\left(p\right) \end{cases} \tag{28}$$

where u_r denotes the output of the ideal non-adaptive version of the $\mathcal{L}_1$ ANN-MPPT controller, given by (23), (21) and (22), and $\eta_r\left(p\right)$ is the Laplace transform of $\eta_r\left(t\right) = w^T\psi\left(\pi_r\right)$.

Remark 3. *The closed-loop reference system (28) describes the desired system dynamics, assuming all uncertainties are known. Furthermore, the control law u_r is purely theoretical and used only for analytical purposes, as they depend on the unknown quantities Δ and w. It is worth noting that the proposed $\mathcal{L}_1$ ANN-MPPT controller follows this ideal closed-loop reference system in both transient and steady-state phases.* ⊡

Lemma 1. Assuming that both the design parameter λ and the filter $C\left(p\right)$ satisfy the $\mathcal{L}_1$-norm condition specified in (27), the following bound holds for all $\tau > 0$ with respect to the closed-loop reference system representation in (28)

$$\left\|\sigma_r\right\|_{\mathcal{L}_\infty} \leq \rho_r \tag{29}$$

where $\rho_r = \frac{\left\|Q(p)\right\|_{\mathcal{L}_1}\left(\epsilon^\star + L_0\right) + \left\|M(p)\right\|_{\mathcal{L}_1}\epsilon^\star + \left\|\sigma_n(p)\right\|_{\mathcal{L}_\infty}}{1 - \left\|Q(p)\right\|_{\mathcal{L}_1}L_1}$. ■

Proof . By replacing u_r with it expression from (28), we obtain

$$\sigma_r\left(p\right) = Q\left(p\right)\eta_r\left(p\right) + M\left(p\right)\epsilon_r\left(p\right) + \sigma_n\left(p\right) \tag{30}$$

where $\sigma_n\left(p\right) = M\left(p\right)\sigma_0$ and $\epsilon_r\left(p\right)$ is the Laplace transform of $\epsilon\left(\pi_r\right)$. Given that the transfer functions $M\left(p\right)$, $Q\left(p\right)$ and $C\left(p\right)$ are proper and BIBO-stable, and that $\sigma_n\left(t\right)$ is uniformly bounded, it follows from (28) and (26) that $\left\|\sigma_r\right\|$, can be upper bounded on $t \in [0, \tau]$ as follows:

$$\left\|\sigma_{r\tau}\right\|_{\mathcal{L}_\infty} \leq \left\|Q\left(p\right)\right\|_{\mathcal{L}_1}\left\|\eta_{r\tau}\right\|_{\mathcal{L}_\infty} + \left\|M\left(p\right)\right\|_{\mathcal{L}_1}\epsilon^\star + \left\|\sigma_{n\tau}\right\|_{\mathcal{L}_\infty} \tag{31}$$

From (19) and (26), an upper bound for $\eta_{r\tau}\left(t\right)$ can be determined as follows:

$$\left\|\eta_{r\tau}\right\|_{\mathcal{L}_\infty} = \left\|H - \epsilon\left(\pi_r\right)\right\|_{\mathcal{L}_\infty} \leq \epsilon^\star + L\left\|\sigma_{r\tau}\right\|_{\mathcal{L}_\infty} + L_0 \tag{32}$$

By substituting (32) into (31) and solving the resulting inequality for $\left\|\sigma_{r\tau}\right\|_{\mathcal{L}_\infty}$, we obtain:

$$\left\|\sigma_{r\tau}\right\|_{\mathcal{L}_\infty} \leq \frac{\left\|Q\left(p\right)\right\|_{\mathcal{L}_1}\left(\epsilon^\star + L_0\right) + \left\|M\left(p\right)\right\|_{\mathcal{L}_1}\epsilon^\star + \left\|\sigma_n\left(p\right)\right\|_{\mathcal{L}_\infty}}{1 - \left\|Q\left(p\right)\right\|_{\mathcal{L}_1}L} \tag{33}$$

Therefore, if the $\mathcal{L}_1$-norm condition in (27) is satisfied, $\left\|\sigma_{r\tau}\right\|_{\mathcal{L}_\infty}$ remains uniformly bounded for all $\tau > 0$, which confirms the inequality in (29). This concludes the proof.

■

4.2 Transient and steady-state performance

In the following, we conduct a performance analysis of the resulting closed-loop dynamics system (20) using the proposed controller outlined in (23), (21) and (22), with a focus on both transient and steady-state behaviors. This analysis is conducted in comparison to the well-behaved closed-loop reference system depicted in (28). Initially, we establish the prediction error dynamics by subtracting (20) from (21), which results in the following expression :

$$\dot{\tilde{\sigma}} = -\beta\tilde{\sigma} - \tilde{\Delta}u + \tilde{w}^T\psi(\pi) - \epsilon(\pi) \tag{34}$$

with $\tilde{\Delta} = \hat{\Delta} - \Delta$ and $\tilde{w} = \hat{w} - w$ are the estimation errors. Additionally, the error dynamics in (34) can be expressed in the frequency domain as

$$\tilde{\sigma}(p) = M(p)\left(\tilde{\eta}(p) - \epsilon(\pi)\right) \tag{35}$$

where $\tilde{\eta}(p)$ is the Laplace transforms of $\tilde{\eta}(t) = -\tilde{\Delta}u + \psi^T(\pi)\tilde{w}$.

Lemma 2. Assuming that the $\mathcal{L}_1$-norm condition described in (27) is satisfied for the system given by (8), which is controlled by the $\mathcal{L}_1$ ANN controller specified in (21)–(23), the following result is obtained:

$$\|\tilde{\sigma}\|_{\mathcal{L}_\infty} \leq \sqrt{\mu_0} \tag{36}$$

with

$$\mu_0 = \frac{1}{\Gamma}\left(4\underset{w\in\Phi}{max}\|w\| + (g_2 - g_1)^2\right) + \gamma^{-1}\epsilon^{\star 2} \tag{37}$$

where $\gamma = (2\beta - 1)$ and $\beta > \frac{1}{2}$. ■

Proof . Let us select the candidate Lyapunov function in the following form

$$V = \tilde{\sigma}^2 + \frac{1}{\Gamma}\tilde{w}^T\tilde{w} + \frac{1}{\Gamma}\tilde{\Delta}^2 \tag{38}$$

Using (34), the time derivative $\dot{V}$ of (38) is as follows

$$\dot{V} = -2\beta\tilde{\sigma}^2 + 2\tilde{w}\left(\tilde{\sigma}\psi^T(\pi) + \frac{1}{\Gamma}\dot{\hat{w}}\right) - 2\tilde{\sigma}\epsilon(\pi) + 2\tilde{\Delta}\left(-\tilde{\sigma}u + \frac{1}{\Gamma}\dot{\hat{\Delta}}\right) \tag{39}$$

From (26) and (22), we can establish an upper limit for $\dot{V}$ such that

$$\dot{V} \leq -2\beta\tilde{\sigma}^2 + 2\tilde{w}\left(Proj\left(\hat{w}, -\tilde{\sigma}\psi(\pi)\right) + \tilde{\sigma}\psi(\pi)\right) + 2|\tilde{\sigma}|\epsilon^\star + 2\tilde{\Delta}\left(Proj\left(\hat{\Delta}, \tilde{\sigma}u\right) - \tilde{\sigma}u\right) \tag{40}$$

Once we consider the properties of the projection operator (see Appendix B), the inequality (40) transforms into:

$$\dot{V} \leq -2\beta\tilde{\sigma}^2 + 2|\tilde{\sigma}|\epsilon^\star \tag{41}$$

or

$$\dot{V} \leq -\gamma\tilde{\sigma}^2 + \epsilon^{\star 2} \tag{42}$$

By employing the projection operator, we ensure that $\hat{w}(t) \in \Phi$ and $\hat{\Delta}(t) \in \Omega$ for $t \geq 0$, thus leading to:

$$\underset{t\geq 0}{max}\frac{1}{\Gamma}\tilde{w}^T\tilde{w} + \frac{1}{\Gamma}\tilde{\Delta}^2 \leq \frac{1}{\Gamma}4\underset{w\in\Phi}{max}\|w\| + (\bar{g}_2 - \bar{g}_1)^2 \tag{43}$$

Substituting (43) into (42) results in:

$$\dot{V}(t) \leq -\gamma V(t) + \gamma\mu_0. \tag{44}$$

Consequently, if at any time $t_1 > 0$, we have $V(t_1) > \mu_0$, then according to the inequality in (44), it implies that $\dot{V}(t_1) < 0$. Additionally, given $\hat{\sigma}(0) = \sigma(0)$, it is straightforward to verify that $V(0) < \frac{1}{\Gamma_i}\left(4\underset{w\in\Phi}{max}\|w\| + (\bar{g}_2 - \bar{g}_1)^2\right) < \mu_0$. Consequently, $V(t) < \mu_0$ for all $t > 0$. Finally, as $\tilde{\sigma}^2 \leq V(t)$ and $\|\cdot\|_\infty \leq \|\cdot\|$, it follows that$\|\tilde{\sigma}\|_{\mathcal{L}_\infty} \leq \sqrt{\mu_0}$, thereby completing the proof. ■

In Lemma 2, based on the expression for μ_0, it becomes evident that increasing the design parameter β and the adaptation gain Γ can result in a significant reduction in prediction errors. This adjustment enhances the control system's capacity to accurately anticipate deviations from expected outcomes.

Theorem 1. Considering the system described in (8) and (20), the reference system defined by (28) and the $\mathcal{L}_1$ ANN controller consisting of (23), (21) and (22), along with the $\mathcal{L}_1$-norm condition specified in (27), we obtain

$$\begin{aligned}\|\sigma_r - \sigma\|_{\mathcal{L}_\infty} &\leq \zeta_1\\ \|u_r - u\|_{\mathcal{L}_\infty} &\leq \zeta_2\end{aligned} \tag{45}$$

and

$$\lim_{\Gamma\to\infty,\,\epsilon^\star\to 0}(\sigma_r(t) - \sigma(t)) = 0 \tag{46}$$

$$\lim_{\Gamma\to\infty,\,\epsilon^\star\to 0}(u_r(t) - u(t)) = 0 \tag{47}$$

with

$$\zeta_1 = \frac{\|C(p)\|_{\mathcal{L}_1}}{1 - \|Q(p)\|_{\mathcal{L}_1}}\sqrt{\mu_0} + \frac{\left(3\|Q(p)\|_{\mathcal{L}_1} + \|M(p)\|_{\mathcal{L}_1}\right)}{1 - \|Q(p)\|_{\mathcal{L}_1}}\epsilon^\star \tag{48}$$

$$\zeta_2 = \left\|\frac{C(p)}{\Delta}\right\|_{\mathcal{L}_1}(L\zeta_1 + 3\epsilon^\star) + \left\|\frac{M(p)}{\Delta}\right\|_{\mathcal{L}_1}\sqrt{\mu_0} \tag{49}$$

and $M_1(p) = \frac{C(p)}{M(p)}$ is proper stable transfer function. ■

Proof . First, by defining $\eta_w(t) = \psi^T(\pi)w(t)$, we can rewrite the control law in (23) as

$$u = KD(p)\left(-\Delta u + \eta_w(p) + \tilde{\eta}(p)\right) \tag{50}$$

which can be alternatively expressed as follows

$$u = \frac{C(p)}{\Delta}\left(\eta_w(p) + \tilde{\eta}(p)\right) \tag{51}$$

where $C(p)$ is the filter introduced in (24).

By replacing the control law (51) in the dynamics (20), we get

$$\sigma = Q(p)\,\eta_w(p) - M(p)\,C(p)\,\tilde{\eta}(p) + M(p)\,\epsilon(p) + \sigma_n(p) \tag{52}$$

this can be rearranged as follows

$$\sigma = Q(p)\,\eta_w(p) - M(p)\,C(p)\left(\tilde{\eta}(p) - \epsilon(p)\right) + Q(p)\,\epsilon(p) + \sigma_n(p) \tag{53}$$

To obtain the expression for the error between σ_r and σ, we subtract (53) from (30), resulting in

$$\sigma_r - \sigma = Q(p)\,\eta_e(p) + C(p)\,\tilde{\sigma}(p) - Q(p)\,\epsilon(p) + M(p)\,\epsilon_r(p) \tag{54}$$

with $\eta_e(t) = \left(\psi^T(\pi_{ref}) - \psi^T(\pi)\right)w$. Given that the transfer functions $M(p)$, $Q(p)$ and $C(p)$ are BIBO-stable and proper, and based on (54), we conclude that the following upper bound is valid for $t \in [0, \tau]$

$$\left\|(\sigma_r - \sigma)_\tau\right\|_{\mathcal{L}_\infty} \leq \left\|Q(p)\right\|_{\mathcal{L}_1}\left\|\eta_{e\tau}(p)\right\|_{\mathcal{L}_\infty} + \left\|C(p)\right\|_{\mathcal{L}_1}\left\|\tilde{\sigma}_\tau(p)\right\|_{\mathcal{L}_\infty} - \left(\left\|Q(p)\right\|_{\mathcal{L}_1} + \left\|M(p)\right\|_{\mathcal{L}_1}\right)\epsilon^\star \tag{55}$$

Additionally, using (26), an upper bound on $\|\eta_{e\tau}\|_{\mathcal{L}_\infty}$ can be determined as

$$\begin{cases} \left\|\eta_{e\tau}\right\|_{\mathcal{L}_\infty} \leq \left\|\left(\psi^T(\pi_r)\,w - \psi^T(\pi)\,w\right)_\tau\right\|_{\mathcal{L}_\infty} \\ \leq \left\|\left(H|_{\sigma_r} - H|_{\sigma}\right)_\tau\right\|_{\mathcal{L}_\infty} + 2\epsilon^\star \\ \leq L\left\|(\sigma_r - \sigma)_\tau\right\|_{\mathcal{L}_\infty} + 2\epsilon^\star \end{cases} \tag{56}$$

When we substitute (56) into (55) and solve the resulting equation for $\|(\sigma_r - \sigma)_\tau\|$, we obtain

$$\left\|(\sigma_r - \sigma)_\tau\right\| \leq \frac{\left\|C(p)\right\|_{\mathcal{L}_1}}{1 - \left\|Q(p)\right\|_{\mathcal{L}_1}}\left\|\tilde{\sigma}_\tau\right\|_{\mathcal{L}_\infty} + \frac{\left(3\left\|Q(p)\right\|_{\mathcal{L}_1} + \left\|M(p)\right\|_{\mathcal{L}_1}\right)}{1 - \left\|Q(p)\right\|_{\mathcal{L}_1}}\epsilon^\star \tag{57}$$

Thus, $\|(\sigma_r - \sigma)_\tau\| \leq \frac{\|C(p)\|_{\mathcal{L}_1}}{1-\|Q(p)\|_{\mathcal{L}_1}}\sqrt{\mu_0} + \frac{\left(3\|Q(p)\|_{\mathcal{L}_1} + \|M(p)\|_{\mathcal{L}_1}\right)}{1-\|Q(p)\|_{\mathcal{L}_1}}\epsilon^\star$, holds uniformly for all $\tau > 0$, and subsequently results in the first bound in (45).

Similarly, to demonstrate the second bound in (45), we begin by subtracting (51) from (28), yielding

$$u_r(p) - u(p) = \frac{C(p)}{\Delta}\eta_e(p) + \frac{C(p)}{\Delta}\tilde{\eta}(p) \tag{58}$$

It can be inferred from Lemma A.12.1 in Hovakimyan and Cao (2010) that $\frac{C(p)}{\Delta}\tilde{\eta}(p)$ can be expressed as

$$\frac{C(p)}{\Delta}\tilde{\eta}(p) = \frac{1}{\Delta}M_1(p)\,\tilde{\sigma}(p) + \frac{C(p)}{\Delta}\epsilon(p) \tag{59}$$

Note that $M_1(p)$ in (59) is a stable and proper transfer function because $C(p)$ is BIBO-stable and strictly proper. This implies that the errors in (58) can be upper bounded, for $t \in [0, \tau]$, as follows

$$\|(u_r(p) - u(p))_\tau\|_{\mathcal{L}_\infty} \leq \left\|\frac{C(p)}{\Delta}\right\|_{\mathcal{L}_1}\left(L\,\|(\sigma_r - \sigma)_\tau\|_{\mathcal{L}_\infty} + 3\epsilon^\star\right) + \left\|\frac{M_1(p)}{\Delta}\right\|_{\mathcal{L}_1}\sqrt{\mu_0} \tag{60}$$

Lastly, by using (57), we obtain $\|(u_r(p) - u(p))_\tau\|_{\mathcal{L}_\infty} \leq \left\|\frac{C(p)}{\Delta}\right\|_{\mathcal{L}_1}(L\zeta_1 + 3\epsilon^\star) + \left\|\frac{M_1(p)}{\Delta}\right\|_{\mathcal{L}_1}\sqrt{\mu_0}$, which demonstrates the second bound in (45).

For the subsequent part of the proof, it is clear that the function μ_0, as defined in (37), is subject to the following limit $\lim_{\Gamma\to\infty,\,\epsilon^\star\to 0}\mu_0 = 0$, which readily allows us to deduce that $\lim_{\Gamma\to\infty,\,\epsilon^\star\to 0}\zeta_1 = 0$ and $\lim_{\Gamma\to\infty,\,\epsilon^\star\to 0}\zeta_2 = 0$. Thus, $\lim_{\Gamma\to\infty,\,\epsilon^\star\to 0}(\sigma_r(t) - \sigma(t)) = 0$ and $\lim_{\Gamma\to\infty,\,\epsilon^\star\to 0}(u_r(t) - u(t)) = 0$. That complete the proof. ■

Based on the findings of the prior study, we can conclude that if the adaptive gain Γ is chosen to be sufficiently large and the resulting approximation error ϵ is sufficiently small, meaning that the RBF neural network approximate uncertainties, then the proposed $\mathcal{L}_1$ ANN controller can ensure that the signals $\sigma(t)$ and $u(t)$ follow $\sigma_r(t)$ and $u_r(t)$ of the stable system described in (28) during both transient and steady-state periods.

Remark 4. *The filter $C(p)$ is crucial in the developed $\mathcal{L}_1$ ANN controller. Notably, if we set $C(p) = 1$, the transfer function $M_1(p) = \frac{C(p)}{M(p)}$ from (59) simplifies to $M_1(p) = \frac{1}{M(p)}$. This leads to an unbounded norm of the resulting transfer function. Therefore, achieving a uniform performance bound for the control signal is impossible without $C(p)$.* ■

5 Simulation results and discussions

In this section, we will focus on assessing the performance of the proposed $\mathcal{L}_1$ ANN-MPPT controller. The evaluation will be carried out under different conditions of solar irradiance and temperature to determine the controller's effectiveness in tracking the MPP. Additionally, we will compare the performance of the developed $\mathcal{L}_1$ ANN-MPPT controller against traditional MPPT controllers, including P&O, IC, and the PI controller, to highlight its advantages. In this research, a BP3280T solar panel is utilised as the PV generator, capable of delivering a peak power of 280.6 W. The parameters of this panel are presented in Table 1, and its V-I characteristics are depicted in Figure 9 and Figure 14 for various environmental conditions. The details regarding the parameters of the DC-DC converter are enumerated in Table 2. We

opted for a 48V/5.5Ah lithium-ion battery as the storage component, beginning with an initial State Of Charge (SOC) set at 60%.

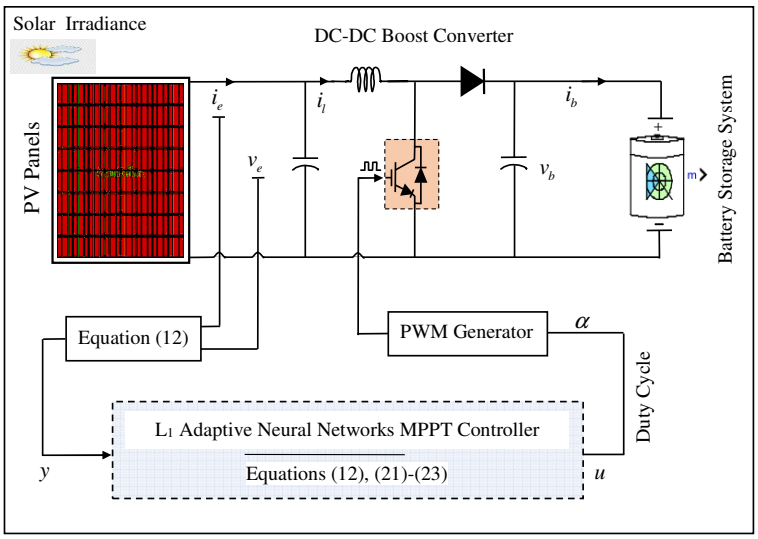


Fig. 3 $\mathcal{L}_1$ ANN-MPPT controller designed for a PV-ES system.

The block diagram illustrating the controlled PV-ES system, along with the proposed $\mathcal{L}_1$ ANN-MPPT controller, is shown in Figure 3. The MPPT controller parameters used in this simulation are specified as follows : $\lambda = 350$, $\beta = 1000$, the adaptation gain $\Gamma = 5 \times 10^5$, and the projection bounds $\hat{\Delta}_i \in [200, 400]$, with $\hat{\Delta}(0) = 0.1$, and $\hat{w}_i \in \left[-5 \times 10^4, 5 \times 10^4\right]$ for $i = 1, \ldots, z$, where $\hat{w}_i(0) = 0$. The feedback gain K and $D(p)$ in the control law (23) are set to $K = 65$ and $D(p) = \frac{1}{p}$. The RBF neural network was configured with an input vector set to $\pi = [y, \dot{y}, u]^T \in \mathbb{R}^3$. The network consists of a total of $z = 200$ nodes, with the width of the Gaussian function fixed at $b_i = 5$ for $i = 1, \ldots, z$. Furthermore, the centre of the receptive vector is set at $a_i \in [-16.5, 16.5]^T$, increasing progressively by 0.1658 for each subsequent node.

The performance assessment of the developed $\mathcal{L}_1$ ANN-MPPT controller is carried out across three scenarios. The initial scenario aims to evaluate its operation under normal weather conditions. The second scenario focuses on the controller's behavior in response to variations in solar irradiation. The third scenario, in turn, assesses its performance in relation to temperature fluctuations. For each scenario, we evaluate the performance in terms of tracking efficiency and response time.

Remark 5. *In practice, the projection intervals* $[\Delta_{\min}, \Delta_{\max}]$ *and the bounds on the neural network weights* w_i *are selected according to the expected operating ranges of the PV voltage, current, and nominal converter parameters. These intervals are chosen wide enough to ensure that the adaptive estimates remain within safe limits, as confirmed through preliminary simulations. Furthermore, the number of neurons in the RBF hidden layer is determined using a compact-domain coverage criterion:*

Table 1 Parameters and specifications of the PV module BP3280T.

Parameters	Notation	Numerical value
Maximum Power	$P_{e_{max}}$	280.6 W
Voltage at maximum power point	$v_{e_{mp}}$	36.2 V
Current at maximum power point	$i_{e_{mp}}$	7.75 A
Open circuit voltage	v_{oc}	44.5 V
Short-circuit current	i_{sc}	8.55 A
Temperature coefficient of i_{sc}	K_{sc}	0.15501 %/°C
Cells per module	n_s	60

Table 2 Specifications of the DC-DC boost converter and the battery energy storage system (Yatimi and Aroudam, 2016).

Parameters	Notation	Numerical value
DC-DC Boost Converter		
Inductance	L_b	2.2 mH
Input capacitor	C_i	47 mF
Output capacitor	C_o	4.7 mF
Switching frequency		20 kHz
Battery energy storage system		
Nominal voltage		48 V
Rated capacity		5.5 AH
Initial SOC		60 %

a sufficient number of Gaussian centers is distributed over the bounded region of the regressor $\pi = [y, \dot{y}, u]^T$ *to provide accurate approximation while maintaining real-time feasibility.* ⊡

5.1 Assessment of performance under normal weather conditions

We begin by evaluating the MPPT performance of the proposed $\mathcal{L}_1$ ANN-MPPT controller under normal weather conditions, characterized by solar irradiation of 1 kW/m^2 and a temperature of 25°C. As illustrated in Figure 9, the MPP under these conditions is $P_{e_{max}} = 208.6$ W and the corresponding voltage and current are $v_{e_{max}} = 36.2$ V and $i_{e_{max}} = 7.75$ A. The simulation results for this scenario are depicted in Figures 4, 5 and 6. In Figure 4 (top), both the theoretical power and the actual output power generated by the PV module are illustrated. Figure 5 displays the controlled output y and the tracking efficiency curve. Meanwhile, Figure 6 showcases the curves of the PV current i_e and the PV voltage v_e. Figure 4 (bottom) shows the time evolution of the SOC.

Figures 4 (top) and 5 show that the proposed MPPT controller provides excellent MPP tracking, achieving a response time of 0.184 sec. and a tracking efficiency of 95.25 %. In addition, this tracking is free of oscillations, as shown in the zoomed-in section of Figure 4 (top), thereby contributing to the stability of the PV-ES system. Figure

6 shows that both the PV voltage v_e and PV current i_e converge to their maximum values $v_{e_{max}}$ and $i_{e_{max}}$. Figure 4 (bottom) shows that the SOC rises linearly starting from 0.2 sec.

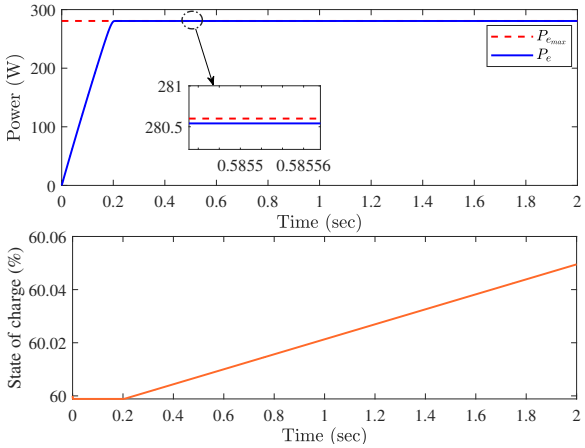


Fig. 4 Analysis performed under normal weather conditions: Top. PV output power P_e and maximum power $P_{e_{max}}$. Bottom. Time evolution of SOC.

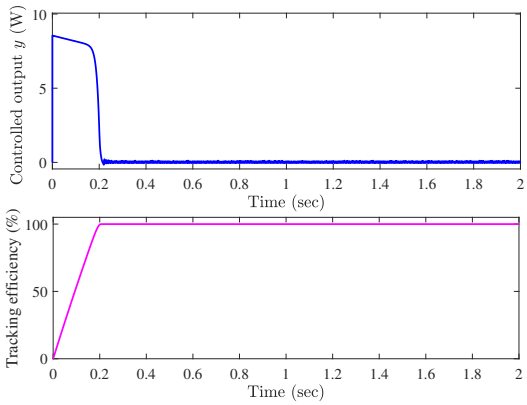


Fig. 5 Analysis performed under normal weather conditions: Top. Controlled output y. Bottom. Tracking efficiency .

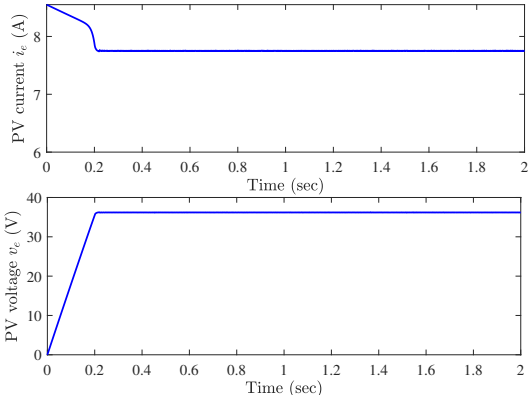


Fig. 6 Analysis performed under normal weather conditions : Top. PV current i_e . Bottom. PV voltage v_e.

5.2 Assessment of performance under irradiance variation

The objective in this scenario is to assess how effectively the suggested $\mathcal{L}_1$ ANN-MPPT controller operates under conditions of rapidly changing solar irradiance. The simulation was performed at different irradiance levels (1000 W/m^2, 500 W/m^2, 800

W/m^2) with the temperature held constant at 25 °C, as displayed in Figure 8. The peak power for each specific irradiance level is depicted in Figure 9.

Figures 7-11 illustrate the results of this scenario. Figures 7 (top) and 10 (top) confirm that the proposed MPPT controller enables fast and precise tracking of the expected MPP, with a rapid response time of 0.231 sec, a tracking efficiency of 93.20%, and no oscillations near the maximum point. Figure 11 shows that the PV voltage v_e and PV current i_e rise or fall in response to each change in solar irradiance levels to instantly track the new MPP. The SOC continuously increased at each irradiance level, displaying different slopes as illustrated in Figure 7 (bottom).

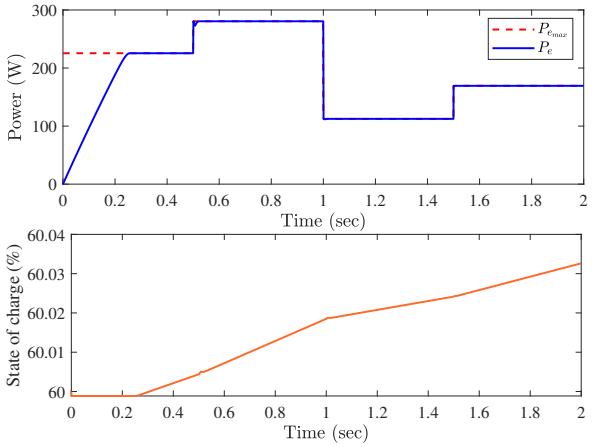


Fig. 7 Analysis performed under varying solar irradiation conditions: Top. PV output power P_e and maximum power $P_{e_{max}}$. Bottom. Time evolution of SOC.

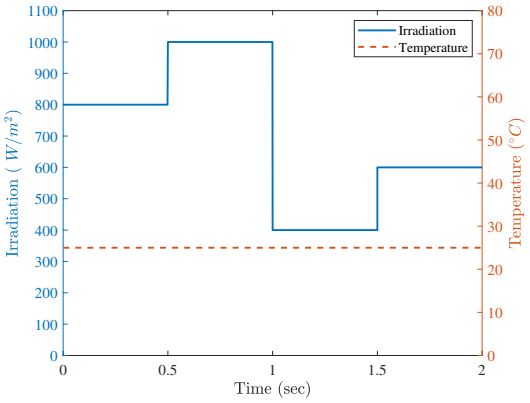


Fig. 8 Overview of variations in solar irradiation conditions at constant temperature.

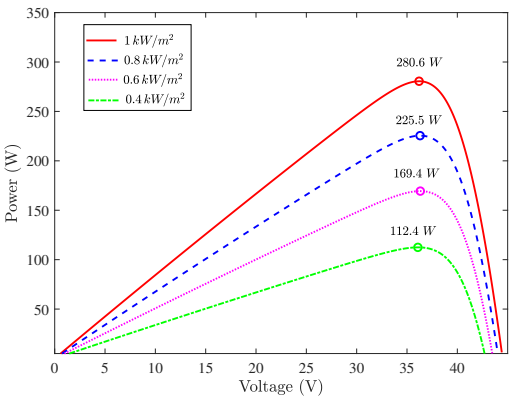


Fig. 9 P-V Characteristic curve of the BP3280T solar panel under various irradiance conditions.

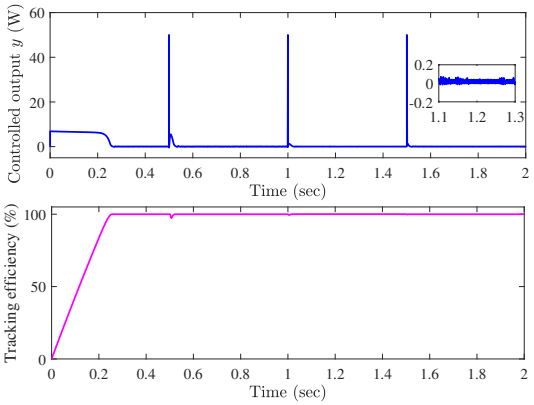


Fig. 10 Analysis performed under varying solar irradiation conditions : Top. Controlled output y . Bottom. Tracking efficiency.

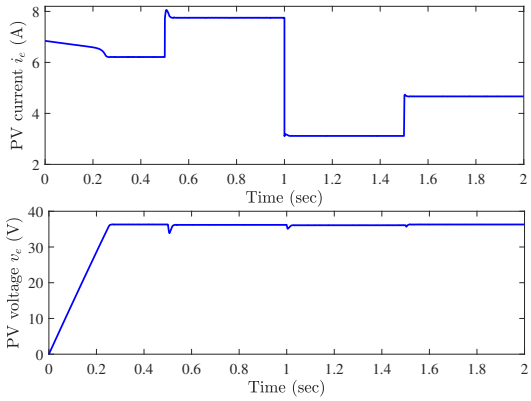


Fig. 11 Analysis performed under varying solar irradiation conditions : Top. PV current i_e . Bottom. PV voltage i_e.

5.3 Assessment of performance under temperature variation

Figure 13 illustrates the temperature change profile considered in this study to evaluate the performance against temperature change. In this assessment, the solar irradiance was kept at 1000 W/m^2 and performance was examined under four distinct temperature conditions: 20°C, 25°C, 35°C, and 40°C. The peak power for each specific temperature value is listed in Figure 14.

Figures 12–16 present the results of this robustness test. Figures 12 (top) and 15 (top) demonstrate the proposed MPPT controller's capability to deliver rapid transient response during sudden temperature changes and Figure 15 (bottom) displays the tracking efficiency, which is 95.14% for this simulation case. From 0 to 0.5 sec, the $\mathcal{L}_1$ ANN-MPPT controller tracks the instantaneous MPP with a response time of 0.184 sec. The response time is 0.02 sec between 0.5 and 1 sec, 0.016 sec between 1 and 1.5 sec, and 0.015 sec between 1.5 and 2 sec. In Figure 12 (bottom), we can observe that even for this test, the SOC value increases continuously from 0.2 sec onward, indicating that the battery is charging but at different rates depending on the temperature.

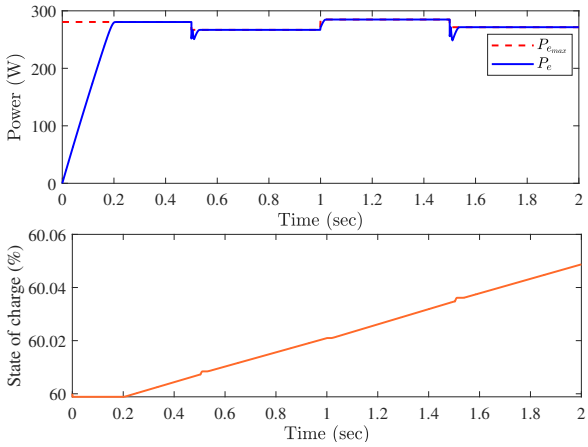


Fig. 12 Analysis performed under varying temperature conditions: Top. PV output power P_e and maximum power $P_{e_{max}}$. Bottom. Time evolution of SOC.

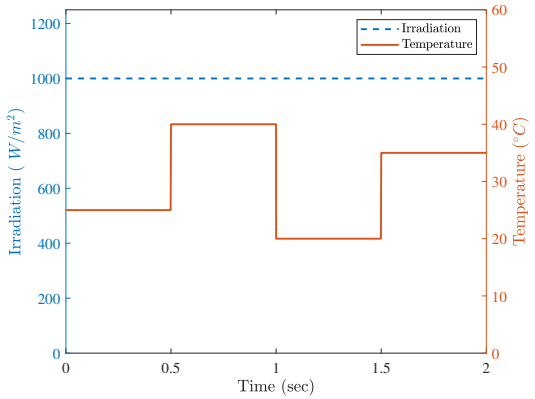


Fig. 13 Depiction of changes in temperature conditions at constant solar irradiation.

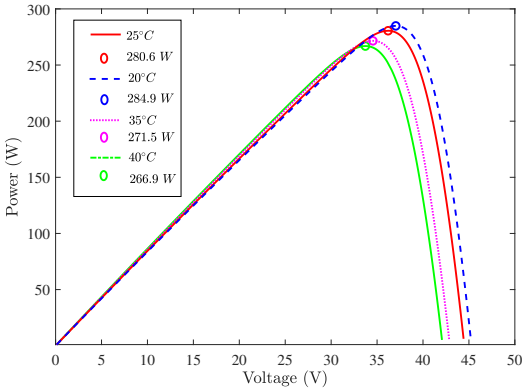


Fig. 14 P-V output curve of the BP3280T solar panel under different temperature conditions.

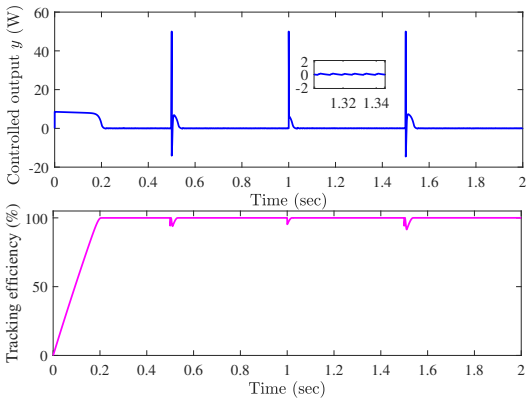


Fig. 15 Analysis performed under varying temperature conditions : Top. Controlled output y . Bottom. Tracking efficiency.

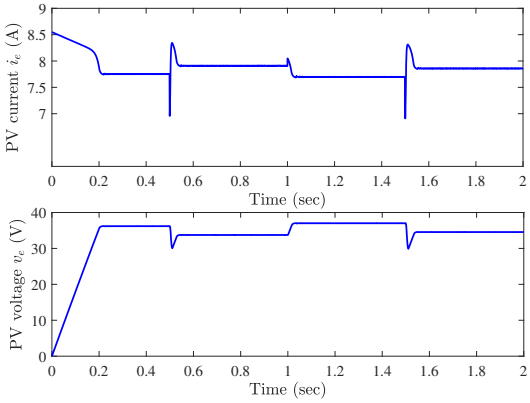


Fig. 16 Analysis performed under varying temperature conditions : Top. PV current i_e . Bottom. PV voltage v_e.

5.4 Comparative Study and Performance Analysis of MPP Tracking

A comparative analysis was carried out to evaluate the performance of the proposed $\mathcal{L}_1$ ANN-MPPT controller against widely used conventional methods, namely P&O, IC, and PI controllers. The comparison was performed under identical conditions—a temperature of 25°C and a solar irradiance of 1000 W/m^2—using the same PV energy storage system parameters to ensure fairness and consistency.

The results, summarized in Table 3 and illustrated in Figures 17 and 18, clearly demonstrate the superior performance of the $\mathcal{L}_1$ ANN-MPPT controller in both transient and steady-state operation. The proposed controller reaches the steady state in approximately 0.18 sec, which is significantly faster than the PI controller whose settling time exceeds 0.26 sec. Furthermore, the $\mathcal{L}_1$ ANN-MPPT controller exhibits a much smoother response with minimal oscillations around the MPP, whereas conventional methods such as P&O, IC, and PI display noticeable fluctuations. These results confirm that the proposed strategy ensures both rapid convergence and reduced steady-state oscillations, thereby offering superior overall performance compared to traditional MPPT techniques.

This superior dynamic behavior is further substantiated by an exhaustive quantitative analysis of steady-state tracking accuracy, as detailed in Table 3. An evaluation of the tracking error ($e_p = p_e - p_{e_{max}}$) over the interval from 0.4 sec to 1 sec reveals the pronounced advantage of the proposed controller. The $\mathcal{L}_1$ ANN-MPPT strategy achieves an average absolute error of merely 0.0593 W, which is approximately four times lower than that of the PI controller (0.2357 W) and over nine times lower than the errors of both the P&O (0.5419 W) and IC (0.5362 W) algorithms. Furthermore, the proposed controller's error range is exceptionally tight, between 0.0590 W and 0.0620 W, demonstrating remarkable stability. In stark contrast, the P&O and IC methods exhibit error ranges exceeding 1.25 W, highlighting their characteristic oscillatory behavior, while the PI controller shows a range of 0.5774 W. The standard

Table 3 Comparative study on MPPT tracking efficiency.

MPPT strategy	Avg (abs(e_p))	Range of e_p	Std of e_p	MPPT Efficiency
$\mathcal{L}_1$ ANN-MPPT controller	0.0593	(0.0590, 0.0620)	4.9106×10^{-4}	99.98
P&O algorithm	0.5419	(0.0590, 1.3320)	0.4510	99.80
IC algorithm	0.5362	(0.0590, 1.2598)	0.4353	99.81
PI controller	0.2357	(0.0590, 0.6364)	0.1559	99.91

deviation of the error for the $\mathcal{L}_1$ ANN controller is a negligible 4.91×10^{-4}, underscoring its consistent precision. This value is over 300 times smaller than that of the PI controller and three orders of magnitude lower than the standard deviations of the P&O and IC methods. Consequently, the $\mathcal{L}_1$ ANN-MPPT controller achieves a peak MPPT efficiency of 99.98%, outperforming all other controllers. These findings quantitatively confirm that the proposed controller successfully eliminates the traditional trade-off between rapid response and steady-state precision, offering unmatched speed, stability, and accuracy for maximum power point tracking.

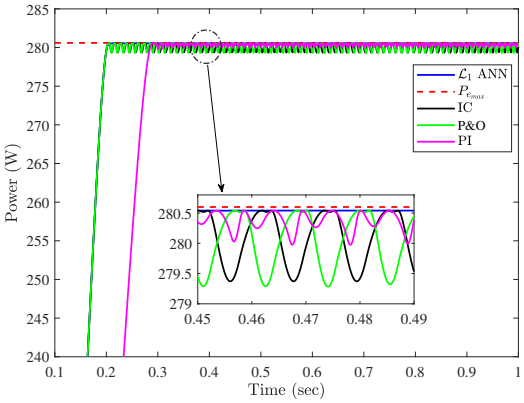


Fig. 17 Tracking performance of the $\mathcal{L}_1$ ANN-MPPT controller compared with conventional MPPT methods.

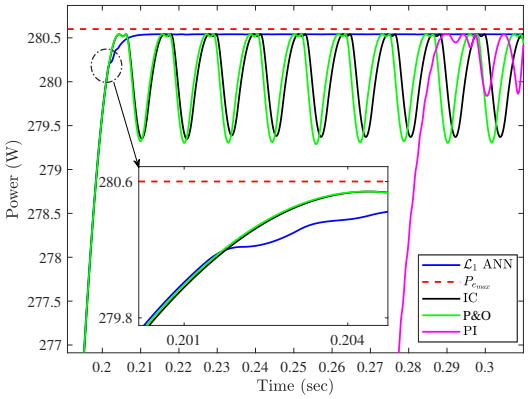


Fig. 18 Dynamic response of the $\mathcal{L}_1$ ANN-MPPT controller compared with conventional MPPT methods.

6 Conclusion

In this study, we have developed an $\mathcal{L}_1$ ANN-MPPT controller for a PV-ES system. The proposed MPPT controller integrates a control law, an adaptive mechanism, a predictor, and an RBF neural network to approximate unknown nonlinear dynamics and uncertainties within the entire system. This new approach ensures rapid adaptation and robust performance, effectively enhancing power extraction from the solar panels and improving battery charging efficiency. Simulation results have demonstrated the MPPT controller's effectiveness and robustness in maximising power extraction from the solar panels, even under fluctuating weather conditions. In addition, the

use of an online-adapted RBF neural network, initialized without any offline training, reinforces the practicality and reproducibility of the proposed MPPT strategy. These findings suggest that the proposed $\mathcal{L}_1$ ANN-MPPT controller represents a significant advancement in enhancing the efficiency and reliability of PV-ES systems, making it a promising solution for future renewable energy applications. In future work, we intend to enhance the proposed $\mathcal{L}_1$ ANN-MPPT controller by incorporating observer-based schemes to improve state estimation and adaptability. Experimental validation will also be carried out to confirm its effectiveness under real-world conditions.

Appendix A

In this appendix, we present some definitions and a lemma that are essential for deriving the main results of this paper.

Definition 1. (Hovakimyan and Cao, 2010; Yoo et al., 2010): Consider a signal $x(t) : [0,\infty) \to \mathbb{R}^n$, we define its truncated $\mathcal{L}_\infty$ norm, denoted as$\|x_t\|_{\mathcal{L}_\infty}$, by $\|x_t\|_{\mathcal{L}_\infty} = \underset{i=1,\ldots,n}{max} (\sup_{0\le\tau\le t} |x_i(\tau)|)$. Similarly, the $\mathcal{L}_\infty$-norm of $x(t)$ is given by $\|x\|_{\mathcal{L}_\infty} = \underset{i=1,\ldots,n}{max} (\sup_{\tau\ge 0} |x_i(\tau)|)$, such that x_i denotes the ith component of x . ■

Definition 2. (Hovakimyan and Cao, 2010; Yoo et al., 2010): For a stable proper SISO system $F(p)$ where p is the Laplace operator, the $\mathcal{L}_1$-norm is defined as $\|F(p)\|_{\mathcal{L}_1} = \int_0^\infty |F(t)|\, dt$, with $F(t)$ being the impulse response of $F(p)$. Moreover, for a strictly proper stable system defined as $y(p) = F(p)\, u(p)$, the following inequality is valid : $\|y_\tau\|_{\mathcal{L}_\infty} \le \|F(p)\|_{\mathcal{L}_1} \|u_\tau\|_{\mathcal{L}_\infty}$. ■

Lemma 3. (Hovakimyan and Cao, 2010): Let $y(p) = F(p)\, u(p)$ represent a continuous-time LTI (proper) system with impulse response matrix $F(t)$. This system is considered BIBO stable if and only if its $\mathcal{L}_1$-norm is bounded, meaning that $\|F\|_{\mathcal{L}_1} < \infty$, or, equivalently, that $F(t) \in \mathcal{L}_1$. ■

Appendix B

In this appendix, we provide the definition of the projection operator (Hovakimyan and Cao, 2010), which is commonly used in adaptive control design.

For two vectors $\theta \in \mathbb{R}^n$ and $\vartheta \in \mathbb{R}^n$, the projection operator $Proj(\cdot,\cdot)$ is described as follows:

$$Proj(\theta,\vartheta) = \begin{cases} \vartheta - \frac{\nabla\mathcal{F}(\theta)\nabla\mathcal{F}^T(\theta)}{\|\nabla\mathcal{F}(\theta)\|^2}\vartheta\mathcal{F}(\theta) & \text{if } \mathcal{F}(\theta) > 0 \text{ and } \nabla\mathcal{F}^T(\theta)\,\vartheta > 0, \\ \vartheta & \text{otherwise,} \end{cases} \tag{61}$$

where $\mathcal{F}(\theta)$ is defined by

$$\mathcal{F}(\theta) = \frac{(\varepsilon_\theta + 1)\,\theta^T\theta - \theta_{max}^2}{\varepsilon_\theta \theta_{max}^2} \tag{62}$$

where $\theta_{max} \in \mathbb{R}^+$ representing the norm bound on the vector θ, and $\varepsilon_\theta \in \mathbb{R}^+$ being the chosen projection tolerance bound.

The projection operator (61) satisfies the following important property

$$(\theta - \theta^{\star})^{T} \left(Proj\left(\theta, \vartheta\right) - \vartheta\right) \leq 0 \tag{63}$$

where θ is the vector being projected, $\theta^{\star}$ is the reference vector (often an optimal or target vector), and ϑ is the vector onto which θ is being projected.

References

Ali, Z.M., Alquthami, T., Alkhalaf, S., Norouzi, H., Dadfar, S., Suzuki, K.: Novel hybrid improved bat algorithm and fuzzy system based MPPT for photovoltaic under variable atmospheric conditions. Sustainable Energy Technologies and Assessments **52**, 102156 (2022) https://doi.org/10.1016/j.seta.2022.102156

Ahmed, M., Harbi, I., Abdelrahem, M., Kennel, R., Rodriguez, J.: Highly efficient MPPT technique using model predictive control. In: 2023 IEEE International Conference on Predictive Control of Electrical Drives and Power Electronics (PRECEDE), pp. 1–5 (2023). https://doi.org/10.1109/PRECEDE57319.2023.10174406 . IEEE

Arsalan, M., Iftikhar, R., Ahmad, I., Hasan, A., Sabahat, K., Javeria, A.: MPPT for photovoltaic system using nonlinear backstepping controller with integral action. Solar energy **170**, 192–200 (2018) https://doi.org/10.1016/j.solener.2018.04.061

Belghiti, H., Kandoussi, K., Harrison, A., Benbba, R., El Otmani, R., Chellakhi, A., Sadek, E.M.: Efficient and robust control of a standalone PV-storage system: An integrated single sensor-based nonlinear controller with TSCC-battery management. Journal of Energy Storage **95**, 112630 (2024) https://doi.org/10.1016/j.est.2024.112630

Boubakir, A., Labiod, S.: Observer-based adaptive neural network control design for projective synchronization of uncertain chaotic systems. Journal of Vibration and Control **29**(15-16), 3658–3678 (2023) https://doi.org/10.1177/10775463221101

Boubakir, A., Labiod, S., Boudjerda, N.: Robust L_1 fuzzy adaptive controller for three-phase grid-connected photovoltaic system. Journal of the Franklin Institute **359**(5), 1852–1880 (2022) https://doi.org/10.1016/j.jfranklin.2022.01.039

Boubakir, A., Labiod, S., Boudjema, F., Plestan, F.: Linear adaptive control of a class of SISO nonaffine nonlinear systems. International Journal of Systems Science **45**(12), 2490–2498 (2014) https://doi.org/10.1080/00207721.2013.772259

Bharti, K.K., Pratima, Patel, A., Jaiswal, Y., Shekhar, Y.: Optimizing solar energy harvesting: A comprehensive review of intelligent MPPT for battery charging circuits. In: 2024 3rd International Conference on Power Electronics and IoT Applications in Renewable Energy and Its Control (PARC), pp. 221–226 (2024). https://doi.org/10.1109/PARC59193.2024.10486254

Boubakir, A., Souanef, T., Labiod, S., Plestan, F., Boudjema, F.: An L_1 fuzzy adaptive controller for a class of SISO nonaffine nonlinear systems: Application to the control of an electropneumatic actuator. Proceedings of the Institution of Mechanical Engineers, Part I: Journal of Systems and Control Engineering **230**(8), 736–748 (2016) https://doi.org/10.1177/0959651816652

Boubakir, A., Touil, S.-A., Labiod, S., Boudjerda, N.: A robust model-free controller for a three-phase grid-connected photovoltaic system based on ultra-local model. Protection and Control of Modern Power Systems **6**, 1–13 (2021) https://doi.org/10.1186/s41601-021-00218-7

Chen, T., Chen, H.: Universal approximation to nonlinear operators by neural networks with arbitrary activation functions and its application to dynamical systems. IEEE transactions on neural networks **6**(4), 911–917 (1995) https://doi.org/10.1109/72.392253

Chen, T., Harrison, A., Alombah, N.H., Aurangzeb, M., Iqbal, S., Mahmoud, H.A.: A simplified control algorithm for efficient and robust tracking of the maximum power point in PV systems. Control Engineering Practice **148**, 105945 (2024) https://doi.org/10.1016/j.conengprac.2024.105945

Chatterjee, H.S., Mahato, S.N.: Simplified p &o MPPT algorithm based performance analysis and control of three-phase IIG-Based MHPCS for remote single-phase household applications. Journal of Control, Automation and Electrical Systems, 1–11 (2024) https://doi.org/10.1007/s40313-024-01118-5

Eltamaly, A.M.: Chapter 4 - performance of MPPT techniques of photovoltaic systems under normal and partial shading conditions. In: Yahyaoui, I. (ed.) Advances in Renewable Energies and Power Technologies, pp. 115–161. Elsevier, Amsterdam (2018). https://doi.org/10.1016/B978-0-12-812959-3.00004-6

El Mezdi, K., El Magri, A., Watil, A., El Myasse, I., Bahatti, L., Lajouad, R., Ouabi, H.: Nonlinear control design and stability analysis of hybrid grid-connected photovoltaic-battery energy storage system with ANN-MPPT method. Journal of Energy Storage **72**, 108747 (2023) https://doi.org/10.1016/j.est.2023.108747

Hovakimyan, N., Cao, C.: L_1 Adaptive Control Theory: Guaranteed Robustness with Fast Adaptation vol. 21. Siam - Society for Industrial and Applied Mathematics, Philadelphia, PA (2010). https://doi.org/10.1137/1.9780898719376

Harrison, A., Dagal, I., Mbasso, W.F., Nguemo Kemdoum, F., Molu, R.J.J., Belghiti, H., Jangir, P.: Real-climatic microcontroller-in-the-loop (RCMIL) framework: A novel, rapid, and cost-effective approach for verifying photovoltaic control systems. Engineering Reports **7**(7), 70285 (2025) https://doi.org/10.1002/eng2.70285

Harrison, A., Farh, H.M.H., Al-Shamma'a, A.A., Mekhilef, S.: An intelligent environmental-sensorless model for real-time optimization in photovoltaic-energy

systems: Fast computation, long-term performance, and experimental validation. Case Studies in Thermal Engineering, 106818 (2025) https://doi.org/10.1016/j.csite.2025.106818

Harrison, A., Mbasso, W.F., Dagal, I., Alombah, N.H., Jangir, P., Al-Gahtani, S.F., Elbarbary, Z.M.S.: Environmental sensor-less hybrid analytical-machine learning (ESHAML) framework for ultra-fast solar irradiance estimation in climate-sensitive real-time applications: experimental validation. Measurement **257**, 118635 (2026) https://doi.org/10.1016/j.measurement.2025.118635

Inthamoussou, F.A., Valenciaga, F.: A fast and robust closed-loop photovoltaic MPPT approach based on sliding mode techniques. Sustainable Energy Technologies and Assessments **47**, 101499 (2021) https://doi.org/10.1016/j.seta.2021.101499

Jately, V., Arora, S.: An efficient hill-climbing technique for peak power tracking of photovoltaic systems. In: 2016 IEEE 7th Power India International Conference (PIICON), pp. 1–5 (2016). https://doi.org/10.1109/POWERI.2016.8077327

Jately, V., Arora, S.: Development of a dual-tracking technique for extracting maximum power from PV systems under rapidly changing environmental conditions. Energy **133**, 557–571 (2017) https://doi.org/10.1016/j.energy.2017.05.049

Jately, V., Arora, S.: Performance investigation of hill-climbing MPPT techniques for PV systems under rapidly changing environment. In: Intelligent Communication, Control and Devices: Proceedings of ICICCD 2017 vol. 624, pp. 1145–1157. Springer, Singapore (2018). https://doi.org/10.1007/978-981-10-5903-2_120

Jately, V., Azzopardi, B., Joshi, J., Venkateswaran V, B., Sharma, A., Arora, S.: Experimental analysis of hill-climbing MPPT algorithms under low irradiance levels. Renewable and Sustainable Energy Reviews **150**, 111467 (2021) https://doi.org/10.1016/j.rser.2021.111467

Jately, V., Bhattacharya, S., Azzopardi, B., Montgareuil, A., Joshi, J., Arora, S.: Voltage and current reference based MPPT under rapidly changing irradiance and load resistance. IEEE Transactions on Energy Conversion **36**(3), 2297–2309 (2021) https://doi.org/10.1109/TEC.2021.3058454

Kaldellis, J.K.: Chapter 13 - photovoltaic-energy storage systems for remote small islands. In: Sørensen, B. (ed.) Solar Energy Storage, pp. 291–326. Academic Press, Boston (2015). https://doi.org/10.1016/B978-0-12-409540-3.00013-X

Kuvshinov, V., Kolomiychenko, V., Kakushkina, E., Ali, L.M.A., Kuvshinova, V.: Storage system for solar plants. Applied Solar Energy **55**, 153–158 (2019) https://doi.org/10.3103/S0003701X19030046

Loukriz, A., Haddadi, M., Messalti, S.: Simulation and experimental design of a new

advanced variable step size incremental conductance MPPT algorithm for PV systems. ISA transactions **62**, 30–38 (2016) https://doi.org/10.1016/j.isatra.2015.08.006

Lashab, A., Sera, D., Guerrero, J.M., Mathe, L., Bouzid, A.: Discrete model-predictive-control-based maximum power point tracking for PV systems: Overview and evaluation. IEEE Transactions on Power Electronics **33**(8), 7273–7287 (2017) https://doi.org/10.1109/TPEL.2017.2764321

Maka, A.O., Chaudhary, T.N.: Performance investigation of solar photovoltaic systems integrated with battery energy storage. Journal of Energy Storage **84**, 110784 (2024) https://doi.org/10.1016/j.est.2024.110784

Mao, M., Cui, L., Zhang, Q., Guo, K., Zhou, L., Huang, H.: Classification and summarization of solar photovoltaic MPPT techniques: A review based on traditional and intelligent control strategies. Energy Reports **6**, 1312–1327 (2020) https://doi.org/10.1016/j.egyr.2020.05.013

Messalti, S., Harrag, A., Loukriz, A.: A new variable step size neural networks MPPT controller: Review, simulation and hardware implementation. Renewable and Sustainable Energy Reviews **68**, 221–233 (2017) https://doi.org/10.1016/j.rser.2016.09.131

Manna, S., Singh, D.K., Akella, A.K., Kotb, H., AboRas, K.M., Zawbaa, H.M., Kamel, S.: Design and implementation of a new adaptive MPPT controller for solar PV systems. Energy Reports **9**, 1818–1829 (2023) https://doi.org/10.1016/j.egyr.2022.12.152

Pourasl, H.H., Barenji, R.V., Khojastehnezhad, V.M.: Solar energy status in the world: A comprehensive review. Energy Reports **10**, 3474–3493 (2023) https://doi.org/10.1016/j.egyr.2023.10.022

Raj, S.A., Samuel, G.G.: Survey of AI based MPPT algorithms in PV systems. In: 2022 4th International Conference on Smart Systems and Inventive Technology (ICSSIT), pp. 597–604 (2022). https://doi.org/10.1109/ICSSIT53264.2022.9716521 . IEEE

Reinders, A., Verlinden, P.J., Sark, W., Freundlich, A.: Photovoltaic Solar Energy: From Fundamentals to Applications, Volume 1. Wiley, Chichester, UK (2017). https://doi.org/10.1002/9781118927496

Sarvi, M., Azadian, A.: A comprehensive review and classified comparison of MPPT algorithms in PV systems. Energy Systems **13**(2), 281–320 (2022) https://doi.org/10.1007/s12667-021-00427-x

Smets, A., Jäger, K., Isabella, O., Swaaij, R., Zeman, M.: Solar Energy: The Physics and Engineering of Photovoltaic Conversion, Technologies and Systems. Bloomsbury Publishing, London (2016)

Slotine, J.-J., Li, W.: Applied nonlinear control. Prentice Hall, Englewood Cliffs, New Jersey (1991)

Safari, A., Mekhilef, S.: Incremental conductance MPPT method for PV systems. In: 2011 24th Canadian Conference on Electrical and Computer Engineering(CCECE), pp. 000345–000347 (2011). https://doi.org/10.1109/CCECE.2011.6030470

Swetha, K., Reddy, V., Robinson, A.: An innovative grey wolf optimizer with Nelder–mead search method based MPPT technique for fast convergence under partial shading conditions. Sustainable Energy Technologies and Assessments **59**, 103412 (2023) https://doi.org/10.1016/j.seta.2023.103412

Sanner, R.M., Slotine, J.-J.E.: Gaussian networks for direct adaptive control. IEEE Transactions on Neural Networks **3**(6), 837–863 (1992) https://doi.org/10.1109/72.165588

Sameera, Tariq, M., Rihan, M., Ayan, M.: A comprehensive review on the application of recently introduced optimization techniques obtaining maximum power in the solar PV system. Renewable Energy Focus **49**, 100564 (2024) https://doi.org/10.1016/j.ref.2024.100564

Tchouani Njomo, A.F., Sonfack, L.L., Douanla, R.M., Kenne, G.: Nonlinear neuro-adaptive control for MPPT applied to photovoltaic systems. Journal of Control, Automation and Electrical Systems **32**, 693–702 (2021) https://doi.org/10.1007/s40313-021-00691-3

Wei, X., Harrison, A., Naser, A.T., Mbasso, W.F., Dagal, I., Alombah, N.H., Jangir, P., Sharaf, M., El-Meligy, M.: A new intelligent control and advanced global optimization methodology for peak solar energy system performance under challenging shading conditions. Applied Energy **390**, 125808 (2025) https://doi.org/10.1016/j.apenergy.2025.125808

Yatimi, H., Aroudam, E.: Assessment and control of a photovoltaic energy storage system based on the robust sliding mode MPPT controller. Solar Energy **139**, 557–568 (2016) https://doi.org/10.1016/j.solener.2016.10.038

Yoo, S.J., Hovakimyan, N., Cao, C.: Decentralised L_1 adaptive control for large-scale non-linear systems with interconnected unmodelled dynamics. IET Control Theory & Applications **4**, 1972–198816 (2010) https://doi.org/10.1049/iet-cta.2009.0526

Yap, K.Y., Sarimuthu, C.R., Lim, J.M.-Y.: Artificial intelligence based MPPT techniques for solar power system: A review. Journal of Modern Power Systems and Clean Energy **8**(6), 1043–1059 (2020) https://doi.org/10.35833/MPCE.2020.000159

DSPACE

https://dspace.org/

Design of a robust adaptive neural network MPPT controller for a photovoltaic energy storage system

Boubakir, Ahsene; Ahmed, Mourad Aït; Labiod, Salim; Souanef, Toufik

2026-12-31
Springer
https://doi.org/10.1007/s40313-025-01234-w
Boubakir A, Ahmed MA, Labiod S, Souanef T. (2026) Design of a robust adaptive neural network MPPT controller for a photovoltaic energy storage system. Journal of Control, Automation and Electrical Systems, Available online 18 January 2026

Downloaded from a DSpace repository. https://dspace.org/